Manganese Oxide Overlayers Promote CO Oxidation on Pt

Siwon Lee, Chao Lin, Seunghyun Kim, Xinyu Mao, Taeho Kim, Sang-Joon Kim, Raymond J. Gorte,* and WooChul Jung*

Cite This: *ACS Catal.* 2021, 11, 13935−13946

Read Online

ACCESS | Metrics & More | Article Recommendations | Supporting Information

ABSTRACT: The influence of manganese oxide on CO oxidation over Pt was investigated. Pt/Al_2O_3 catalysts were modified by the atomic layer deposition (ALD) of MnO_x with deposition before or after addition of Pt, and the results were compared to those with an unmodified Pt/Al_2O_3 catalyst. The addition of MnO_x improved the catalyst durability, mitigating the agglomeration of Pt particles after thermal aging at 1073 K. The addition of MnO_x also promoted CO oxidation rates by creating active $Pt-MnO_x$ interfacial sites despite the fact that CO adsorption was suppressed after high-temperature calcination. Transmission electron microscopy (TEM) showed that Pt was uniformly covered by a thin film of MnO_x after calcination. The implications of these results with regard to understanding the MnO_x promotion of Pt catalysts are discussed.

KEYWORDS: *platinum, manganese oxide, atomic layer deposition, overcoating layer, undercoating layer, CO oxidation*
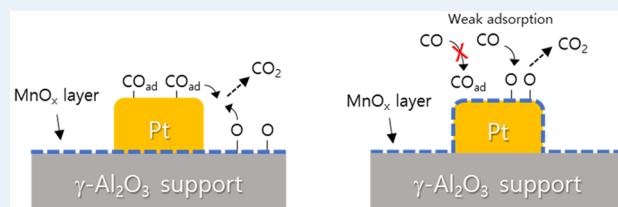
INTRODUCTION

The catalytic oxidation of carbon monoxide is a key reaction in automotive emission control processes, and the reaction over Pt has been studied extensively.[1,2] CO oxidation is usually considered to be insensitive to the structure used, as rates have been shown to scale linearly with the Pt surface area over a very wide range of particle sizes when Pt is supported on nonreducible supports.[3] However, increased rates have been reported for Pt on reducible supports.[4−6] The promotion of rates is most notable with ceria supports[7] where, depending on the temperature and reactant pressures, specific rates for CO oxidation over Pt/ceria can be higher than those for Pt/Al_2O_3 by several orders of magnitude.

Among other reducible oxides, MnO_x is attractive due to its earth abundance, structural versatility, and rich redox chemistry. MnO_x has been shown to promote metal catalysts for a number of reactions, including CO oxidation, toluene oxidation, ethylene oxidation, and the oxidative decomposition of formaldehyde.[4,8−11] However, MnO_x is not sufficiently stable for high-temperature applications, and metals supported on MnO_x tend to deactivate severely due to sintering. It is therefore of interest to us to prepare thermally stable materials that will maintain a good contact between MnO_x and Pt.

Coinfiltration of both a metal and a metal oxide promoter onto a stable support such as Al_2O_3 is the conventional method used to maintain a high surface area in a promoted metal catalyst. However, coinfiltration does not ensure that there will be physical contact between two components. For example, a relatively recent study in which Pd and ceria were infiltrated onto Al_2O_3 showed clear evidence that the ceria and Pd were not in physical contact after calcination, despite the fact that the ceria loading was 22 wt %.[12] In contrast, better physical contact between Pd and ceria was achieved when ceria was added by atomic layer deposition (ALD), and this contact was maintained even after calcination up to 1073 K. Whereas infiltration usually involves the precipitation of a salt from a fluid phase, resulting in the formation of oxide particles that cover only a fraction of the support, ALD produces conformal films on the support, ensuring that there will be contact with the metal catalyst.

ALD produces oxide films that are conformal on the atomic scale by a sequential self-limiting reaction of a metal oxide precursor with the surface, followed by oxidation of the adsorbed precursor. While it was developed primarily for semiconductor fabrication, ALD has also been shown to provide advantages for the synthesis of catalysts that are typically in particulate form.[13] For example, ALD-coated oxide overlayers have been shown not only to stabilize the metal particle size following high-temperature sintering[14−23] but also to facilitate the selective production of desired products.[24,25] In other examples, conformal films of an oxide on a more stable support have exhibited the chemical properties of the film with the stability of the support. The $Pd-ceria-Al_2O_3$ catalyst, discussed above, is one example of this. Metals stabilized by perovskite films are other examples.[26]
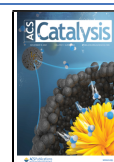
Table 1. Properties of the Samples Used in This Study

| sample | BET surface area (m²/g) | | metal oxide loading (wt %) | Pt loading (wt %) | film thickness (nm) |
	773 K calcined	1073 K calcined			
Al_2O_3		113			
Pt/Al_2O_3	103 ± 6	105 ± 1		4.0	
$MnO_x/Pt/Al_2O_3$	39 ± 5	32 ± 2	30	2.8	0.83
$Pt/MnO_x/Al_2O_3$	89	86	14	3.5	0.29

In this study, we examined MnO_x-promoted Pt/Al_2O_3 catalysts to gain a better understanding of the nature of Pt–MnO_x interactions. Catalysts were prepared with thin MnO_x coatings either on or under the Pt, and the results were compared to those with an unmodified Pt/Al_2O_3 catalyst. Improved thermal stability was observed regardless of the location of the ALD layer. Moreover, Pt–MnO_x interfacial sites were shown to exhibit higher CO oxidation activity levels despite the fact that CO adsorption on MnO_x-overcoated Pt was suppressed after high-temperature aging.

EXPERIMENTAL METHODS

A commercial γ-Al_2O_3 powder (Strem Chemicals, Inc.) was stabilized by thermal aging in air at 1173 K for 24 h and then used as a support for the deposition of Pt and MnO_x. The ALD process was done using a home-built apparatus that is described in the literature.[27] Pt and MnO_x were introduced onto the support by ALD using $Pt(acac)_2$ (Strem Chemicals, Inc.) and $Mn(TMHD)_3$ (tetrakis(2,2,6,6-tetramethyl-3,5-heptanedionato)manganese(III); Strem Chemicals, Inc.) as the precursors. ALD was performed by exposing the evacuated samples to the precursor vapors for 10 min at 573 K, followed by evacuation and subsequent oxidation for 10 min at 773 K. The growth rate for Pt has previously been established as 1.1×10^{14} Pt atoms/(cycle cm²).[28] The growth rate for MnO_x was determined gravimetrically (Figure S1) on both γ-Al_2O_3 and Pt/γ-Al_2O_3 to be 5.8×10^{13} Mn atoms/(cycle cm²) (0.015 nm/cycle, assuming uniform deposition of Mn_3O_4 and the bulk density for the film). After oxide deposition, all samples were subjected to an additional thermal treatment at either 773 or 1073 K for 1 h.

To confirm the Pt ALD growth rate, the chemical composition of the Pt/Al_2O_3 sample was determined by inductively coupled plasma optical emission spectrometry (ICP-OES) (Spectro Genesis spectrometer with a Mod Lichte nebulizer). Prior to the analysis, the sample was dissolved in aqua regia and diluted with deionized (DI) water. MnO_x compositions were calculated from the mass changes in the sample, assuming an oxidation state of Mn_3O_4. Surface areas were determined from Brunauer–Emmett–Teller (BET) isotherms using the N_2 adsorption at 77 K in a home-built system. A summary of some of the key properties of the samples used in this study is reported in Table 1.

Transmission electron microscopy (TEM) and scanning transmission electron microscopy (STEM) analyses were conducted using powder specimens. These were dispersed and sonicated in ethanol and then loaded onto lacey carbon films on copper grids (Electron Microscopy Sciences). The TEM and STEM data together with elemental maps generated via energy dispersive X-ray spectroscopy (EDS) were collected with a Talos F200X (FEI) operated at 200 kV. Aberration-corrected TEM, STEM, and EDS mapping data were collected by means of a Titan cubed G2 60-300 (FEI) instrument operated at 300 kV. The crystal structure of the samples was

characterized by powder X-ray diffraction using a RIGAKU SmartLab diffractometer with Cu Kα irradiation. The surface chemical state of the catalysts was analyzed by X-ray photoelectron spectroscopy (XPS) with a Sigma probe from Thermo Scientific. The analysis was carried out under ultrahigh vacuum (UHV) with Al Kα irradiation.

CO chemisorption experiments were conducted with a home-built adsorption apparatus and an AutoChem II 2920 analyzer from Micromeritics, assuming the adsorption of one CO molecule per surface Pt atom. For chemisorption, the samples were oxidized at 673 K for 10 min in air, reduced in H_2 (200 Torr) at 423 K for 10 min, and then evacuated. The reduction and evacuation processes were repeated three times. CO chemisorption was performed at 298 K. Diffuse-reflectance infrared Fourier-transform spectroscopy (DRIFTS) spectra were collected on a Nicolet iS50 FTIR spectrometer from Thermo Fisher Scientific. The spectral resolution was 4 cm^{-1}, and the scan number was 32 for each spectrum. The samples were prepared by mixing KBr and each sample at a ratio of 9:1, and a total of 100 mg of the mixture was placed in a crucible. The samples were cleaned under an oxygen atmosphere by flowing a 10% O_2–90% He mixture at 573 K for 1 h and then reduced under a 5% H_2–95% He mixture at the same temperature and duration of time. After it was cooled to 298 K, the chamber was purged for 30 min by flowing N_2 at a rate of 40 mL min^{-1}. The vibrational spectra under CO oxidation were obtained over a period of 20 min by flowing a CO (4%) and O_2 (2%) gas mixture balanced in He. The spectra under CO desorption were then collected for 20 min by flowing N_2 gas. The total flow rate of each experiment was adjusted to 40 mL min^{-1}, and the measurements were conducted at both 323 and 423 K.

Temperature-programmed reduction (TPR) experiments were conducted with an AutoChem II 2920 analyzer from Micromeritics. The catalysts were oxidized at 573 K for 2 h under a 10% O_2–90% He mixture. After the sample was cooled to 323 K, a 10% H_2–90% He mixture was introduced onto the sample and the temperature was increased to 1123 K at 10 K min^{-1}. The total flow rate was kept at 50 mL min^{-1}. A thermal conductivity detector (TCD) was used to measure the amount of H_2 consumed. The temperature-programmed desorption (TPD) experiments utilized a quadrupole mass spectrometer (GSD320) from PFEIFFER Vacuum. The samples were oxidized at 773 K for 30 min under a 5% O_2–95% Ar mixture and cooled to 323 K. After that, TPD operation was carried out under an Ar gas flow at a rate of 100 mL min^{-1}. The temperature was increased to 1073 K at a rate of 8 K min^{-1}. The oxygen that desorbed from the sample was monitored with a mass spectrometer signal, 32.

CO oxidation rates were assessed in a quartz-tube flow reactor with an inner diameter of a 1/4 in. For all measurements, we used 100 mg of the catalyst loaded between two plugs of quartz wool to avoid displacement of the catalyst. The feed to the reactor consisted of 28 Torr of CO and 14 of
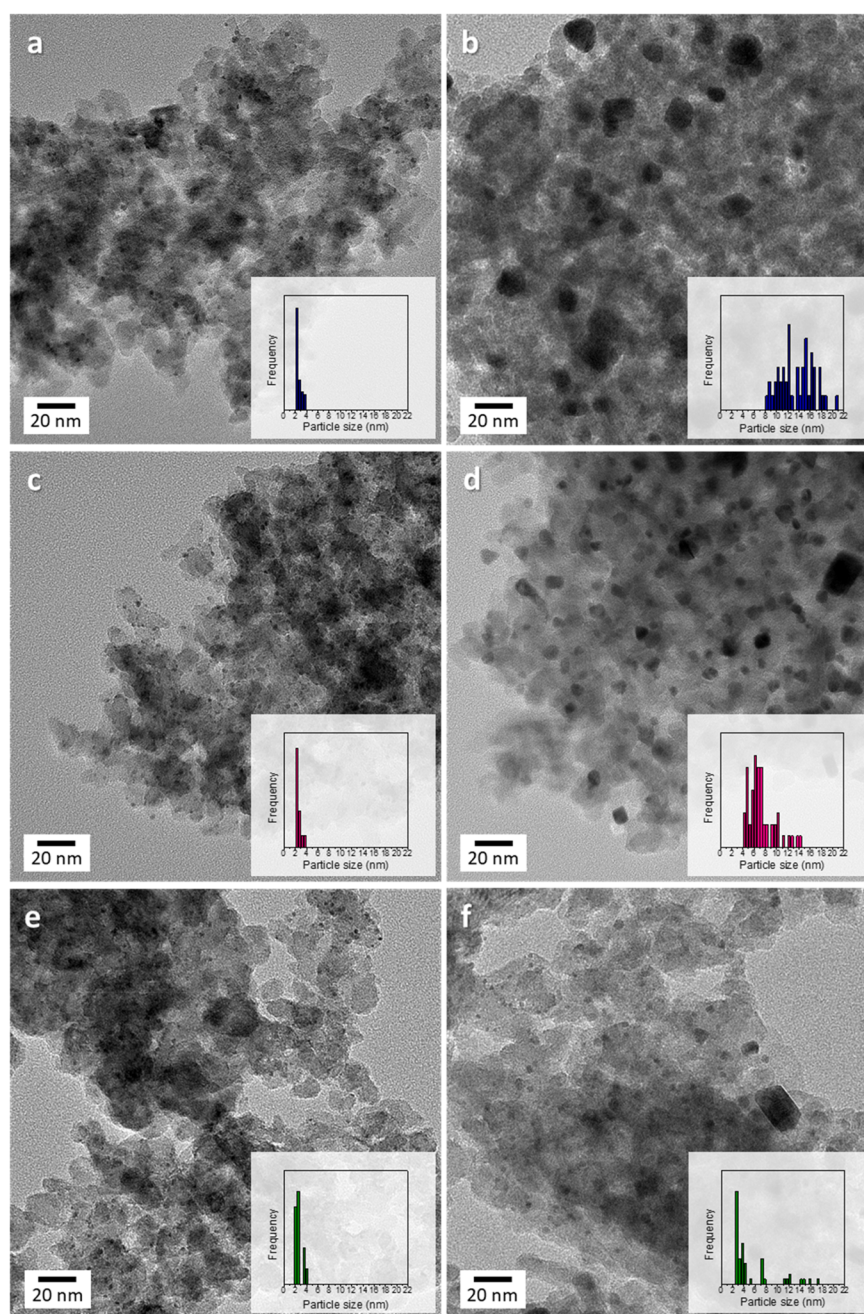
Figure 1. TEM images of Pt/Al_2O_3, $Pt/MnO_x/Al_2O_3$, and $MnO_x/Pt/Al_2O_3$ catalysts after various pretreatments: Pt/Al_2O_3 heat-treated at (a) 773 K and (b) 1073 K; $Pt/MnO_x/Al_2O_3$ heat-treated at (c) 773 K and (d) 1073 K; $MnO_x/Pt/Al_2O_3$ heat-treated at (e) 773 K and (f) 1073 K. The inset of each figure shows the particle-size distribution.

Torr O_2, with the balance being He. The total flow rate was maintained at 106 mL min^{-1}. The products were detected with an online gas chromatograph (SRI8610C) equipped with a HayeSep Q column and a TCD detector. Before the rate measurements, the catalysts were activated at 573 K in H_2 (5%) for 1 h. Differential conditions were maintained at all times, and the reported rates were normalized to the mass of Pt in the samples.

■ RESULTS

To determine the effect of MnO_x on the Pt activity and stability, the three samples given in Table 1 were examined. The Pt/Al_2O_3 sample was conventional except for the fact that

Pt was added by one ALD cycle of the $Pt(acac)_2$ precursor. The $Pt/MnO_x/Al_2O_3$ sample had a Mn_3O_4 loading of 0.16 g of Mn_3O_4/g Al_2O_3, which corresponds to an average film thickness of 0.29 nm assuming that the film has the bulk density of Mn_3O_4 and that it uniformly covers the 113 m^2/g Al_2O_3 surface. A previous study suggested that this MnO_x loading is sufficient to achieve uniform coverage on Al_2O_3.[29] The added mass of the MnO_x film decreased the BET surface area slightly, which in turn resulted in a somewhat lower Pt loading, as the amount of Pt added in one ALD cycle is proportional to the surface area. The $MnO_x/Pt/Al_2O_3$ sample had a Mn_3O_4 loading of 0.43 g of Mn_3O_4/g of Pt/Al_2O_3, which corresponds to an average film thickness of 0.83 nm assuming that the film covers the Pt/Al_2O_3 surface at 105 m^2/g. A
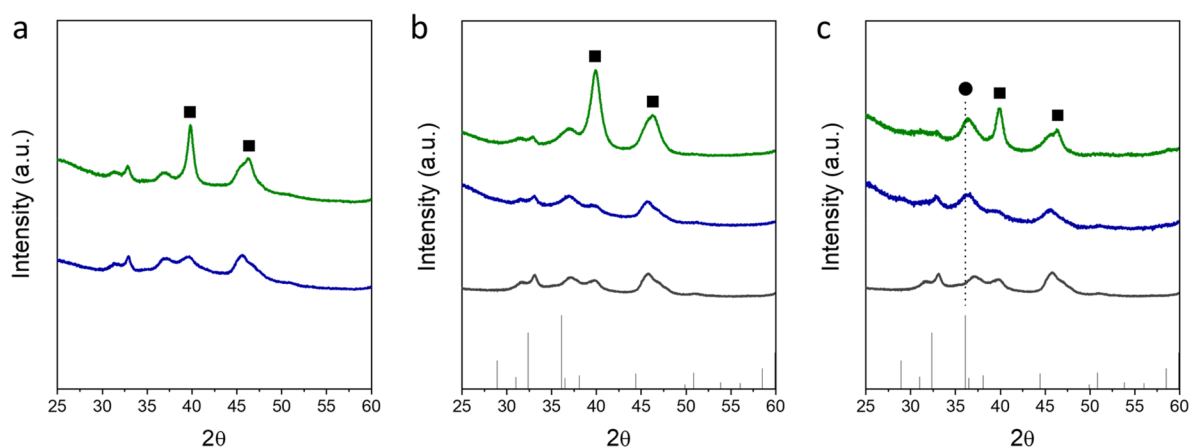
Figure 2. XRD patterns of (a) Pt/Al_2O_3, (b) $Pt/MnO_x/Al_2O_3$, and (c) $MnO_x/Pt/Al_2O_3$ catalysts prepared under different conditions: each catalyst after a thermal treatment for 1 h at 773 K (blue) and 1073 K (green). The XRD pattern of the pristine γ-Al_2O_3 support is indicated by the gray lines. The pattern at the bottom in (b) and (c) is the XRD pattern of Mn_3O_4 (JCPDS 80-0382) included here for reference. Characteristic peaks for Pt and MnO_x are denoted by the square symbols and by the circle symbol, respectively.

Table 2. Dispersion Values for Various Samples after Thermal Aging at Different Temperatures

	samples					
	$Pt/MnO_x/Al_2O_3$		$MnO_x/Pt/Al_2O_3$		Pt/Al_2O_3	
thermal aging condition	measd[a]	estimated[b]	measd[a]	estimated[b]	measd[a]	estimated[b]
773 K	32	290	12 ± 2	130	56 ± 7	50
1073 K	13 ± 1	97	3 ± 1	50	8	8

[a]Dispersion values measured by CO chemisorption measurements. [b]Dispersion values estimated from the specific reaction rate of CO oxidation as reported in the literature.[3]

thicker film layer was used in this case to ensure encapsulation of the Pt particles, similar to what was reported in a previous study with ZrO_2 films on Pd/Al_2O_3.[30]

Figure 1 shows TEM images of these three samples after calcination at 773 and 1073 K, while the corresponding EDS maps are reported in Figures S2 and S3. The Pt/Al_2O_3 sample heated to 773 K (Figure 1a) shows a narrow Pt particle-size distribution centered at about 3 nm. Heating to 1073 K (Figure 1b) resulted in a significant growth of the metal particles and broadening of the particle-size distribution, with most of the Pt particles ranging in size from 8 to 20 nm. TEM bright-field images of $Pt/MnO_x/Al_2O_3$ (Figure 1c) and $MnO_x/Pt/Al_2O_3$ (Figure 1e) calcined at 773 K were nearly identical with that of Pt/Al_2O_3. The bright-field images showed no evidence of MnO_x in these samples, although the corresponding EDS maps showed a uniform distribution of Mn in both cases. The only change that occurred when these samples were calcined to 1073 K was the growth of the Pt particles. The average diameters were 7.3 ± 2.4 nm for $Pt/MnO_x/Al_2O_3$ (Figures 1d) and 5.4 ± 3.9 nm for $MnO_x/Pt/Al_2O_3$ (Figures 1f). The presence of MnO_x clearly suppressed Pt sintering, especially when it was added as an overlayer.

XRD patterns for these three samples after oxidation at either 773 or 1073 K are shown in Figure 2. The patterns for all three samples were essentially identical following calcination at 773 K. Each showed small, broad features attributable to metallic Pt. An estimate of the Pt particle size from the Scherrer equation gave values between 3 and 4 nm (Table S1) for each of the samples, in good agreement with the TEM results. The failure to find features associated with any MnO_x phase on the $Pt/MnO_x/Al_2O_3$ and $MnO_x/Pt/Al_2O_3$ samples is consistent with the fact that the MnO_x films were thinner than

the coherence length of the X-rays in both samples. After calcination to 1073 K, the diffraction peaks associated with Pt grew significantly on each of the samples. The calculated particle sizes were 13.0 nm for Pt/Al_2O_3 and 8.3 nm for $Pt/MnO_x/Al_2O_3$, in reasonable agreement with the TEM observations. For $MnO_x/Pt/Al_2O_3$, the Pt crystallite size was calculated and found to be 11.9 nm, which is significantly larger than the TEM value of 5.4 nm. Because there was a wide distribution of particle sizes in that sample, it is likely that the larger Pt particles contributed more to the XRD line width. It is important to note that, even after high-temperature treatments, only the $MnO_x/Pt/Al_2O_3$ sample showed possible evidence of a diffraction feature at ~37° 2θ, which could be associated with MnO_x.

As a final check of the Pt particle size and dispersion, CO chemisorption measurements were taken, as reported in Table 2. On Pt/Al_2O_3, the initial dispersion was 57%, in good agreement with the measured 3 nm particle size; this decreased to 8% after calcination at 1073 K. For the MnO_x-modified Pt, before the measurement, we checked that no CO adsorption occurred in the MnO_x/Al_2O_3 without Pt (Figure S4). The initial dispersion on $Pt/MnO_x/Al_2O_3$ was 32%, lower than 57% but still representing Pt particles with an average size of 3−4 nm. The dispersion decreased less, to 14%, after heating to 1073 K, in agreement with the 7−8 nm size observed by TEM. Finally, CO uptake levels on $MnO_x/Pt/Al_2O_3$ were only 13% after calcination at 773 K and 2% after 1073 K. These correspond to Pt particle sizes of 9 and 36 nm, respectively; however, this is not true on consideration of the TEM data. The apparently low dispersions on this MnO_x-overcoated sample indicate that the Pt must at least be partially encapsulated. In earlier work with ZrO_2 films on Pd/Al_2O_3,
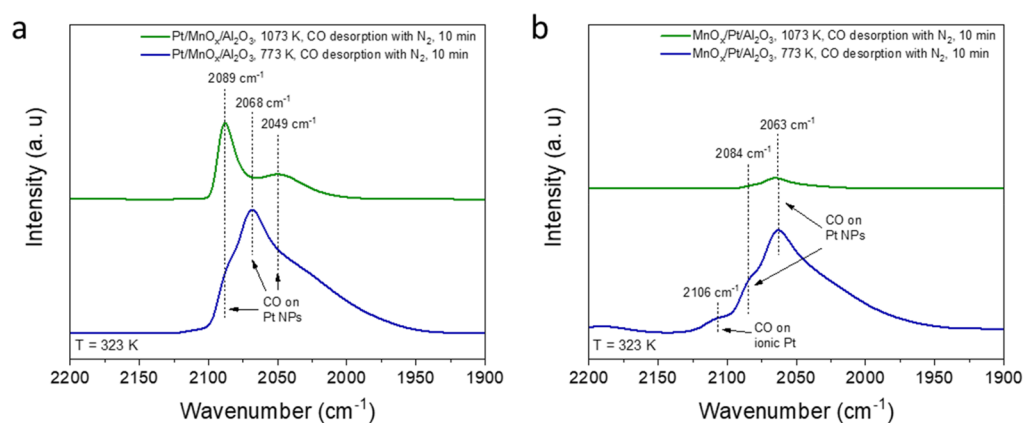
Figure 3. Diffuse reflective infrared Fourier-transform spectroscopy (DRIFTS) spectra collected for (a) $Pt/MnO_x/Al_2O_3$ and (b) $MnO_x/Pt/Al_2O_3$ catalysts after calcination at 773 and 1073 K. The samples were exposed to a CO (4%) and O_2 (2%) gas mixture balanced in He for 20 min at 323 K. After 10 min of CO desorption, the vibrational spectra were obtained.
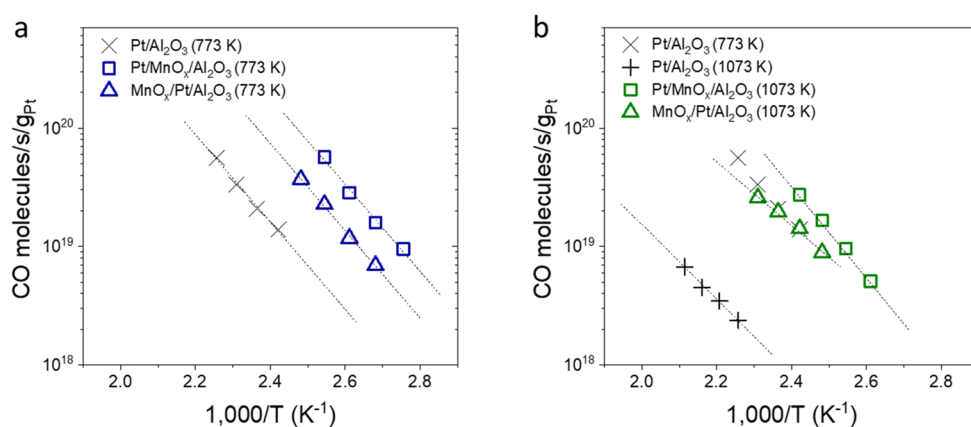

Figure 4. Reaction rates for CO oxidation with 28 Torr of CO and 14 Torr of O_2 for Pt/Al_2O_3, $MnO_x/Pt/Al_2O_3$, and $Pt/MnO_x/Al_2O_3$ catalysts (a) before and (b) after thermal aging at 1073 K.

high-temperature treatments exposed the Pd by breaking up the oxide overlayer.[30] High temperatures appear to have had the opposite effect with MnO_x.

Diffuse-reflectance infrared Fourier-transform spectroscopy (DRIFTS) was utilized to determine whether the MnO_x changed the nature of the CO bonding to the Pt. As shown in Figure 3, the $Pt/MnO_x/Al_2O_3$ sample exhibited features associated with CO adsorption on Pt/Al_2O_3, with bands at 2089, 2068, and 2049 cm^{-1}.[31,32] The tail extending to lower wavenumbers can be attributed to CO bound to Pt atoms of different coordination types and/or sizes.[33] For $MnO_x/Pt/Al_2O_3$ calcined at 773 K, the vibrational spectrum still showed CO adsorption features on Pt. However, in agreement with the very low CO uptake levels, the $MnO_x/Pt/Al_2O_3$ catalyst showed weak features related to CO adsorbed on Pt after aging at 1073 K.

Differential rates for CO oxidation were measured on each of the three samples in 28 Torr of CO and 14 Torr of O_2, with Arrhenius plots being reported in Figure 4a for samples calcined at 773 K and in Figure 4b after calcination at 1073 K. Rates on the MnO_x-containing samples were significantly higher on the 773 K samples, even though the apparent activation energy (E_a) values were similar at approximately 70 kJ/mol. Although the different rate processes cannot be simply identified on the basis of the apparent value of E_a, at least we can say that because the E_a values are similar, the rate

difference can be explained by the difference in the pre-exponential factor and/or reaction orders under a given reaction condition. After calcination at 1073 K, the rates on Pt/Al_2O_3 decreased dramatically, whereas the effect of the high-temperature treatments on the two MnO_x-containing samples was much more modest. This trend was identical even after aging at 1073 K for 24 h (Figure S5), demonstrating the stability of our catalytic system. Because the rates on MnO_x itself are very low (see Figure S6), MnO_x must act to promote a reaction on the Pt, like other TMOs. In comparison to the various Pt/TMOs reported in the literature, our MnO_x-modified Pt catalysts exhibited similar CO oxidation activity levels, except for some Pt/CoO_x catalysts (Figure S7).

Rates on unpromoted Pt have been reported to increase linearly with the Pt surface area;[3] therefore, one way to quantify the effects of MnO_x promotion is to estimate the Pt dispersions using the Pt surface area calculated from the CO oxidation rates on unpromoted catalysts. As shown in Table 2, the dispersions estimated this way for Pt/Al_2O_3 were in very good agreement with the dispersions measured from CO chemisorption after calcination at both 773 and 1073 K. However, the dispersions calculated from the reaction rates for the MnO_x-containing samples were between 7 and 16 times higher than those determined from CO chemisorption. Clearly, MnO_x promotes the reaction in addition to stabilizing the catalyst.
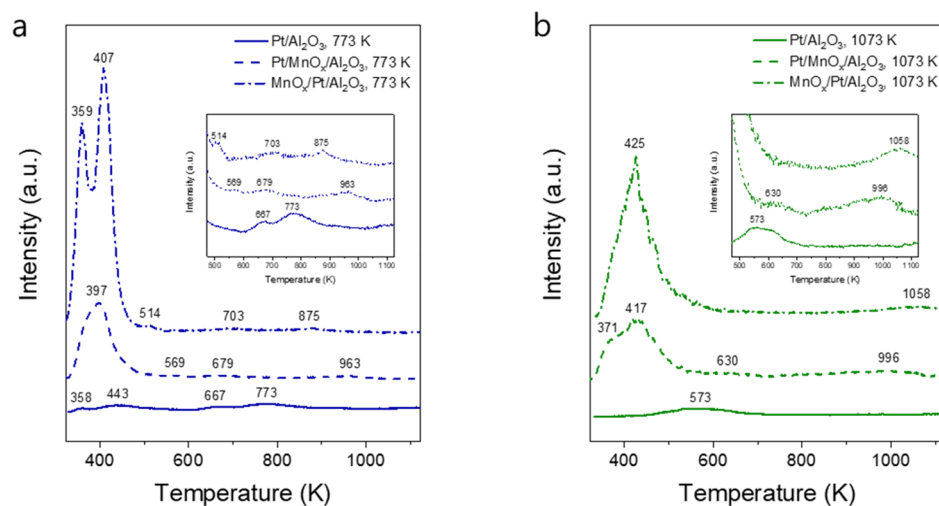
Figure 5. H$_2$-TPR profiles of samples after calcination at 773 and 1073 K.
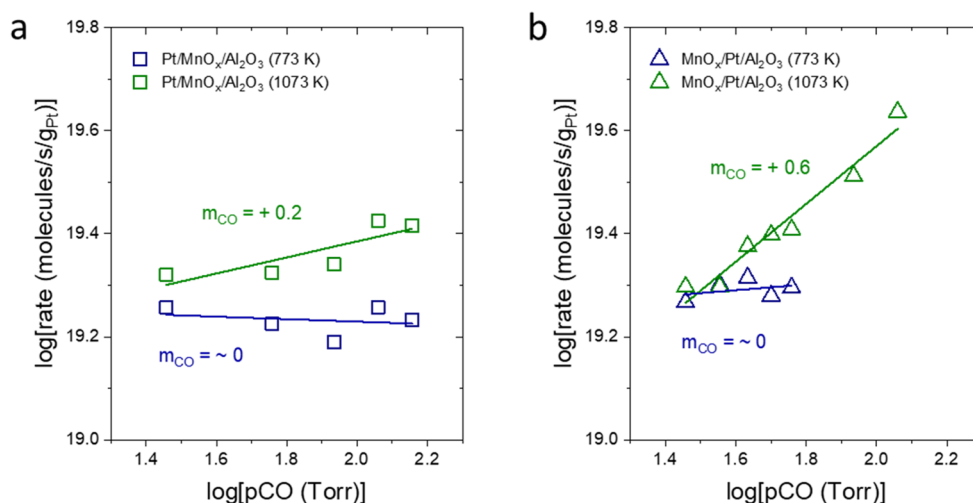

Figure 6. Reaction orders with respect to CO in (a) Pt/MnO$_x$/Al$_2$O$_3$ and (b) MnO$_x$/Pt/Al$_2$O$_3$ catalysts before and after thermal aging.

To identify the promotion of MnO$_x$ to Pt further, the reducibility of the samples was studied by the H$_2$ temperature-programmed reduction (TPR) technique (Figure 5). Pt/Al$_2$O$_3$ heated to 773 K showed four unresolved peaks at 358, 443, 667, and 773 K mainly due to the reduction of different species of PtO$_x$. The first two peaks below 573 K are assigned to the weakly interacting PtO$_x$ species, and the other two peaks at higher temperatures stem from the reduction of PtO$_x$ strongly interacting with the support.[34] After heating at 1073 K, the reduction behavior of the Pt site was changed and the reduction occurred with a broad peak near 547 K. In all cases, the reduction was not as prominent. After the introduction of MnO$_x$, the reducibility of the catalyst was greatly enhanced. For Pt/MnO$_x$/Al$_2$O$_3$ heated to 773 K, it showed a strong peak at 397 K with several small peaks at 569, 679, and 963 K. In general, peak evolution in the range of 523−823 K is linked to MnO$_x$ reduction to MnO, and that above 900 K is assigned to the reduction of Mn ions strongly bound to the support.[34,35] Therefore, the newly observed reduction behavior at 397 K should be the result of the promotion effect between MnO$_x$ and Pt. The promotion effect continued after calcination at 1073 K. For MnO$_x$/Pt/Al$_2$O$_3$, the reducibility was improved further. After heating to 773 K, the reduction profile showed

two characteristic peaks at 359 and 407 K, indicating that there were energetically different reduction sites due to the promotion effect. The sample heated to 1073 K exhibited a single peak at 425 K with high intensity. Although the peak at a low temperature of 359 K disappeared, still it shows strong reducibility due to the promotion. The apparently stronger reducibility in MnO$_x$-overcoated Pt catalysts is likely due to the large amount of MnO$_x$ in contact with Pt.

Changes in the reaction order for CO oxidation have been observed on transition metals that are in contact with reducible oxides, such as ceria,[36,37] Co$_3$O$_4$,[15] and SmMn$_2$O$_5$;[46] therefore, we investigated the reaction orders for CO and O$_2$ on the present samples. For Pt/Al$_2$O$_3$, these were approximately −1 for CO and +1 for O$_2$, regardless of thermal aging, in agreement with the standard Langmuir−Hinshelwood (LH) mechanism for CO oxidation on Pt (Figure S8).[38] However, for the MnO$_x$-containing samples, the reaction orders for CO were significantly different, as shown in Figure 6. On Pt/MnO$_x$/Al$_2$O$_3$, as shown in Figure 6a, the rates were nearly independent of the CO partial pressure following calcination at either 773 or 1073 K. On MnO$_x$/Pt/Al$_2$O$_3$, as shown in Figure 6b, the reaction order was significantly positive after calcination at 1073 K. Previous reports with other promoters

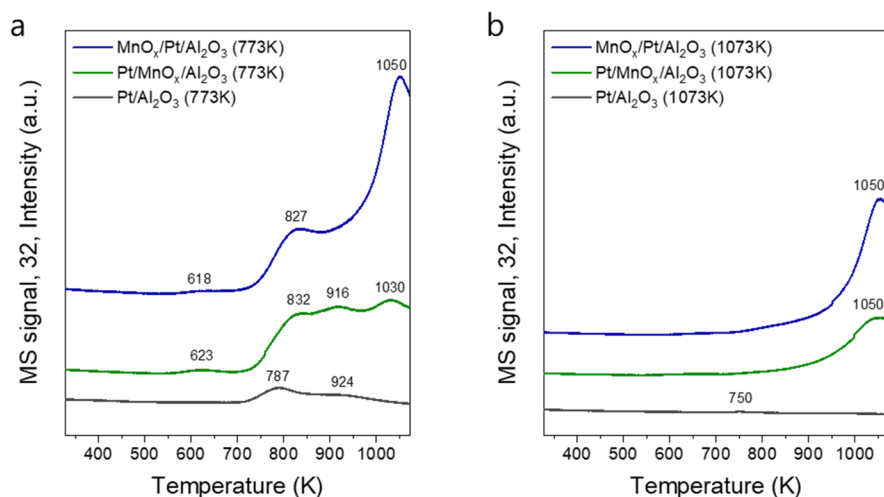**Figure 7.** O_2-TPD profiles of samples after calcination at (a) 773 K and (b) 1073 K.
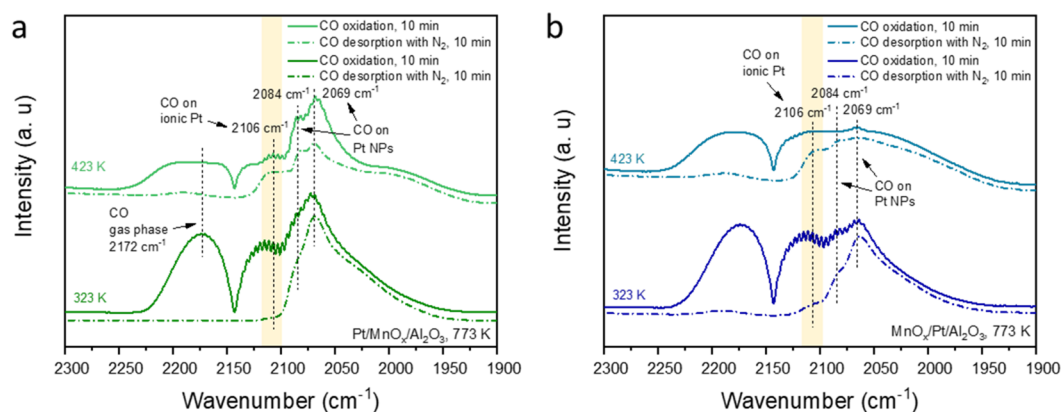

Figure 8. *In situ* diffuse-reflectance infrared Fourier-transform spectroscopy (DRIFTS) spectra on (a) $Pt/MnO_x/Al_2O_3$ and (b) $MnO_x/Pt/Al_2O_3$ catalysts under CO oxidation (solid line) and desorption with N_2 (dash-dotted line) at temperatures of 323 and 423 K. The catalysts were calcined to 773 K before the measurement. After 10 min of CO oxidation and desorption, the vibrational spectra were obtained. The wavenumber region for CO adsorbed on ionic Pt is highlighted in yellow.

have argued that the change in reaction order is due to an enhanced reaction at the metal−oxide interface.[39,40] If oxygen originates from the oxide, high coverages of CO on the metal will not poison the reaction. This also appears to occur in MnO_x-containing catalysts.

In this regard, the desorption state of oxygen in the catalysts was studied with temperature-programmed desorption (TPD) (Figure 7). The Pt/Al_2O_3 catalyst heated to 773 K showed two desorption peaks above 700 K (Figure 7a, gray line), whereas heating to 1073 K led to a significant reduction in the desorption signal (Figure 7b, gray line), mainly due to the growth of Pt particles. The desorption profiles of $Pt/MnO_x/Al_2O_3$ and $MnO_x/Pt/Al_2O_3$ calcined at 773 K showed much stronger intensities in comparison to that of Pt/Al_2O_3. Both exhibit several energetically different O species between 600 and 1073 K. Notably, $MnO_x/Pt/Al_2O_3$ showed strong oxygen evolution at a high temperature of ∼1050 K (Figure 7a, blue line). Given that surface-adsorbed oxygen is desorbed at low temperatures and the oxygen released at higher temperatures (>773 K) is related to lattice oxygen,[41] MnO_x-modified Pt catalysts appear to facilitate the release of lattice oxygen. After heating to 1073 K, the desorption profile intensity levels were decreased overall but were still stronger than those of Pt/Al_2O_3 (Figure 7b). Although the type of released oxygen appears to

vary with the catalyst structure and thermal aging condition, we clearly identified that MnO_x facilitates the supply of oxygen species.

In situ diffuse-reflectance infrared Fourier-transform spectroscopy (DRIFTS) was conducted while the reaction temperatures were varied to gain further insights into the reaction mechanism. Figure 8 shows the vibrational spectra of the $MnO_x/Pt/Al_2O_3$ and $MnO_x/Pt/Al_2O_3$ catalysts after heating to 773 K. At a temperature of 323 K, both catalysts showed bands at ∼2084 and ∼2069 cm^{-1}, which are associated with CO adsorption on Pt NPs as discussed above. For $MnO_x/Pt/Al_2O_3$, a small shoulder band also appeared at 2106 cm^{-1}, which can be ascribed to CO adsorbed on ionic Pt.[42,43] CO gas bands were also observed under the CO oxidation condition. After the temperature was increased to 423 K, CO was oxidized to CO_2, as evidenced by the decreased level of CO gas and the adsorption band features as well as the increase in CO_2 bands (2333−2361 cm^{-1}, Figure S9). In addition, a band at 2106 cm^{-1} increased during the reaction for both samples. This shows that Pt became oxidized, losing electrons during the reaction process. Meanwhile, the ionic Pt does not appear in Pt/Al_2O_3 (Figure S10). Therefore, it is reasonable that electrons from Pt were transferred to MnO_x. Because the reduction process of MnO_x (accepting electrons) causes the
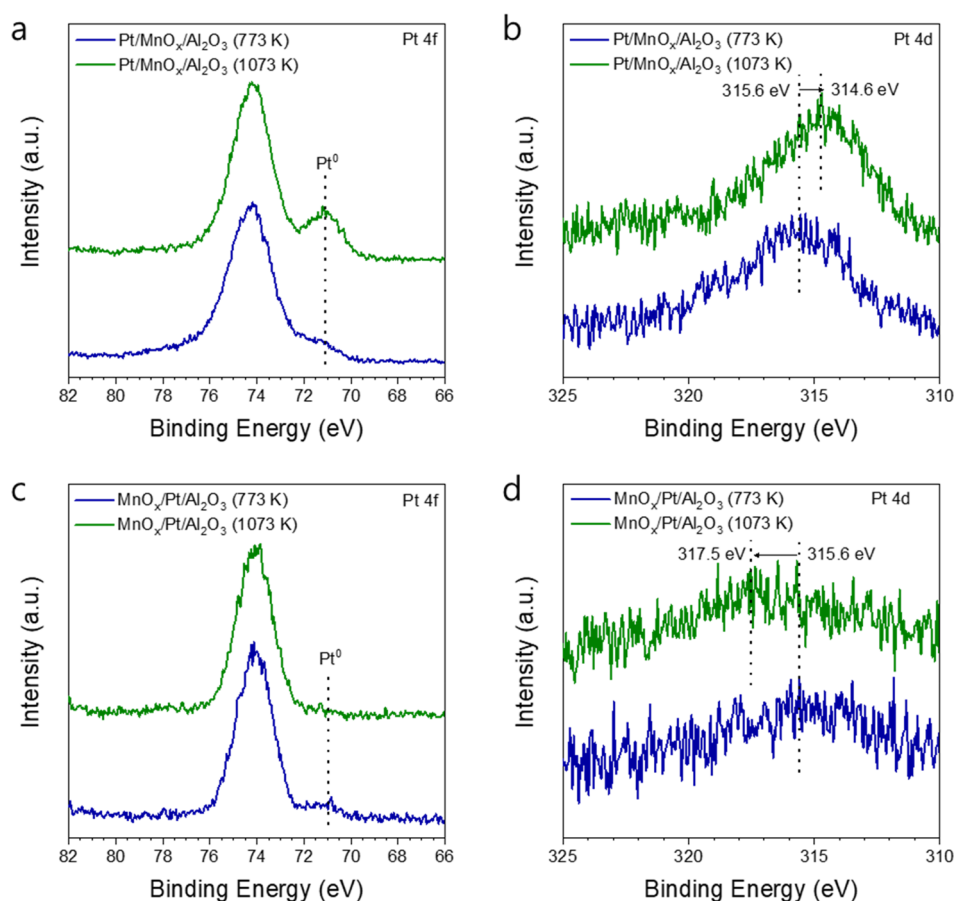
Figure 9. XPS Pt 4f and 4d spectra of Pt/MnO$_x$/Al$_2$O$_3$ and MnO$_x$/Pt/Al$_2$O$_3$ after calcination at 773 and 1073 K.

release of oxygen, this observation suggests that MnO$_x$ likely supplies oxygen during the CO oxidation, which enhances the activity. Interestingly, despite the low CO uptake levels, the MnO$_x$-overcoated Pt aged at 1073 K also showed the formation of ionic Pt (Figure S11). This indicates that a similar reaction mechanism is operating in the MnO$_x$-modified catalysts. When these findings were taken together, we found that the ionic Pt formation can indicate the interaction between MnO$_x$ and Pt and that the improved activity is likely related to the activation of oxygen at the Pt–MnO$_x$ interface.

For a more in-depth study of the metal–oxide interaction, the chemical state of Pt was examined by means of an X-ray photoelectron spectroscopy (XPS) analysis. Figure 9 shows the Pt 4f and 4d spectra on Pt/MnO$_x$/Al$_2$O$_3$ and MnO$_x$/Pt/Al$_2$O$_3$. In Figure 9a, Pt/MnO$_x$/Al$_2$O$_3$ heated to 773 K shows a spectrum with two characteristic peaks. The spectrum is the result of overlapping Al 2p and Pt 4f spectra. A large peak at ~74.3 eV comes from Al$_2$O$_3$, and a shoulder peak at 71.2 eV is for Pt metal (Pt^0). After the sample was heated to 1073 K, the Pt metal peak became larger. In the corresponding Pt 4d spectra (Figure 9b), the peak position shifted to a lower binding energy from 315.6 to 314.6 eV after heating to 1073 K, which again indicates that Pt became more metallic with a lower oxidation state. This is due to the grain growth of Pt during the high-temperature treatment. Meanwhile, the MnO$_x$/Pt/Al$_2$O$_3$ sample showed the opposite trend. In Figure 9c, the metallic Pt peak at ~71.2 eV became smaller after heating to 1073 K. The Pt 4d spectra exhibited a corresponding peak shift to a higher binding energy from 315.6 to 317.5 eV (Figure 9d). The higher oxidation state of Pt

indicates more cationic Pt species, likely due to the improved interaction between Pt and MnO$_x$ upon thermal aging. As will be mentioned later, this result suggests that a large portion of Pt comes into contact with MnO$_x$; thus, the Pt–MnO$_x$ interface is maximized. The presence of this type of interface explains why this catalyst is still active without strong CO adsorption.

To gain a better understanding of the Pt–MnO$_x$ interface, the MnO$_x$-containing samples that had been calcined to 1073 K were investigated more thoroughly using aberration-corrected, high-resolution TEM (HR-TEM). Images of the MnO$_x$/Pt/Al$_2$O$_3$ catalyst aged at 1073 K, together with EDS maps, are shown in Figure 10 and Figure S12. These clearly indicate a thin and uniform crystalline MnO$_x$ layer on the surface of the Pt particle. This fact supports the higher oxidation state of Pt observed in XPS. The MnO$_x$ film was less than 1 nm thick and appears to consist of a few atomic layers with a lattice spacing of approximately 0.37 nm (Figure 10h). As shown in Figure S13, this overlayer was also observed in smaller Pt particles. Additional evidence that the overlayer consists of MnO$_x$ comes from the fact that the image brightness of the Pt particles is darker than that of the surface layer. Given that the brightness is inversely proportional to the atomic number, the overlayer must be composed of a material with an atomic number lower than that of Pt. The appearance of the MnO$_x$ film and the suppression of CO adsorption are reminiscent of the strong metal–support interaction (SMSI) behavior observed with titania-supported metals; however, unlike SMSI, which is induced by high-temperature reduction, the overlayer in this case is produced during an oxidation
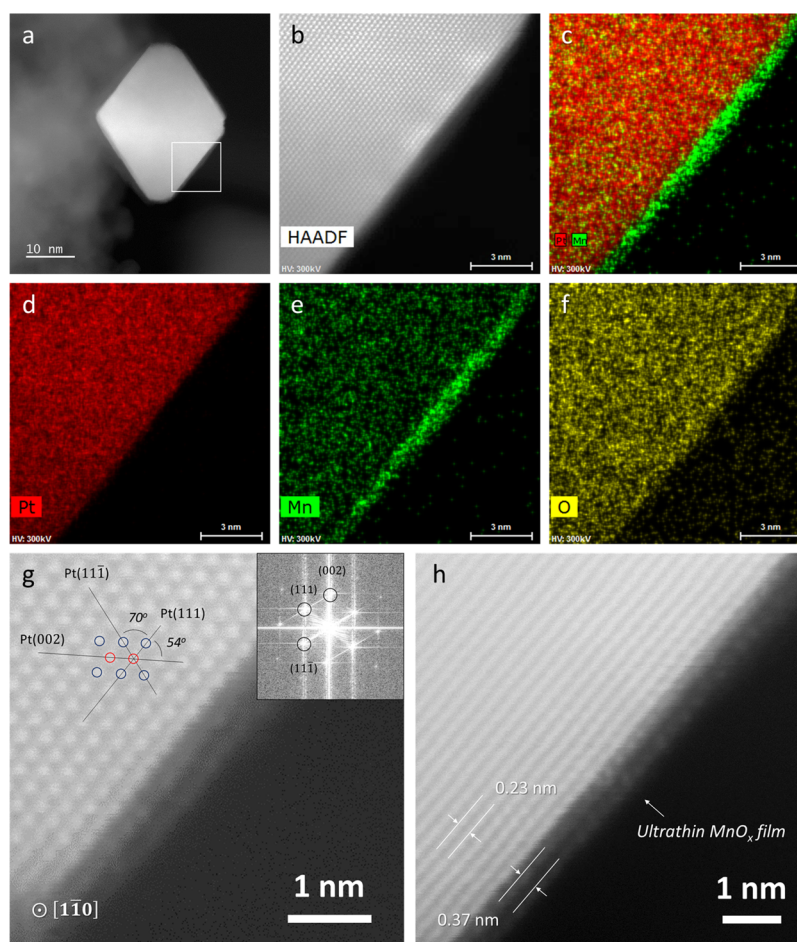
Figure 10. (a) Representative STEM image of $MnO_x/Pt/Al_2O_3$ after thermal aging for 1 h at 1073 K. (b) Magnified STEM image of the boxed area in (a) with (c–f) EDS maps of Pt, Mn, and O. (g) Magnified STEM of the (b) image and the (g, inset) corresponding fast Fourier-transform (FFT) pattern. The zone axis of Pt is $[1\bar{1}0]$, with (111), $(11\bar{1})$, and (002) facets parallel to the zone axis and electron beam. The plane angles of $\langle(111), (11\bar{1})\rangle$ and $\langle(111), (002)\rangle$ are 70 and 54°, respectively. (h) Magnification of the STEM image shown in (b) focused on the MnO_x layer. The interplanar distances of the two atomic layers of MnO_x and Pt(111) are ~3.70 and ~2.30 Å, respectively.

process. We also performed HR-TEM on the $Pt/MnO_x/Al_2O_3$ catalyst aged at 1073 K, the results of which are shown in Figure S14. In this case, we were not able to observe the MnO_x overlayer directly on this sample. The fact that only $MnO_x/Pt/Al_2O_3$ formed a thin film of MnO_x after aging suggests that the MnO_x initially deposited on Pt played a role in driving the structural evolution.

DISCUSSION

In this study, we have shown that MnO_x promotes CO oxidation over Pt catalysts. MnO_x appears to do so by donating oxygen to CO on the Pt. Long-range electronic effects are unlikely to play a major role in these materials, especially after calcination at 1073 K, as the metal particles were relatively large.[44] Therefore, good interfacial contact between the MnO_x and Pt appears to be critically important to achieve this promotion. As discussed elsewhere,[12] ALD is ideal for preparing materials with maximum MnO_x–Pt contact because the oxide support can be produced as a conformal film.

The fact that MnO_x forms a well-defined film on Pt particles and is stable even after calcination at 1073 K implies that there must be bonding interactions between the Pt and MnO_x. The formation of the film must minimize the free energy of the system. This is somewhat unusual, given that oxides do not

normally "wet" metals. It is possible that the Mn in these films exists in a oxidation state lower than that of the expected Mn_2O_3 due to these interactions; however, spectroscopic identification would be difficult because most of the MnO_x in these samples would not be in contact with Pt. It would be interesting to perform model studies of MnO_x on Pt films to clarify the nature of these interactions. The stability of the MnO_x film may also explain the reduced sintering of Pt particles in these catalysts.

There is clearly much that we do not know about the effect of MnO_x on Pt. Understanding how the catalyst prepared by depositing MnO_x overlayers on Pt/Al_2O_3 could be active for CO oxidation but not exhibit strong adsorption features of CO is especially challenging. The TEM images appear to indicate that the oxide overlayers completely cover the Pt; however, the fact that MnO_x itself showed very low activity in comparison to Pt would imply that must be gaps in that oxide overlayer. The sites associated with those gaps would be similar to the Pt–MnO_x interface and must be very active for the rates to remain high. Another possible explanation is that the ultrathin oxide film exhibits catalytic activity during the CO oxidation reaction. However, in this case, only MnO_x in the localized region near Pt can be involved, and this phenomenon is primarily seen in oxides within a few atomic distances from the

metal.[44,45] Thus, we propose that the reaction still proceeds at the Pt−MnO$_x$ interface sites. The reducibility, oxygen desorption profile, Pt chemical states, and *in situ* observation of the vibrational spectra support the presence of such oxide−metal interfaces. Meanwhile, we suggest that the catalyst prepared by the deposition of Pt onto the MnO$_x$ film had both "normal" Pt sites and interfacial sites. The presence of normal sites is demonstrated by room-temperature CO chemisorption and CO vibrational spectra similar to those expected for conventional Pt/Al$_2$O$_3$, while the zeroth order for CO, *in situ* DRIFTS, O$_2$-TPD, and H$_2$-TPR analysis findings imply that interfacial sites are still important in the MnO$_x$-undercoated Pt.

The different roles of MnO$_x$, either above or below the metal, may provide a unique perspective on catalyst design strategies. In particular, the ability of nongas adsorption in conjunction with oxidation for CO in the "oxide-on-metal" catalyst suggests that this is a potentially useful structure for research involving the selective operation of only a desired reaction while unwanted side reactions on metal surfaces are suppressed.[46]

■ CONCLUSION

The introduction of ALD-MnO$_x$ overlayers on or underneath Pt improved the thermal stability and CO oxidation activity of the conventional Pt/Al$_2$O$_3$ catalyst. The addition sequence of the ALD-MnO$_x$ played a role in altering the reaction sites. Pt on MnO$_x$ showed both normal Pt sites and Pt−MnO$_x$ interface sites, whereas MnO$_x$ on Pt was dominated by interface sites. In the MnO$_x$-overcoated Pt, a thin and uniform crystalline MnO$_x$ layer covered the Pt surface after high-temperature oxidative firing. Nonetheless, the CO oxidation reaction was still promoted, implying that the Pt−MnO$_x$ interface is important for the reaction.

■ ASSOCIATED CONTENT

Ⓢⓘ Supporting Information

The Supporting Information is available free of charge at https://pubs.acs.org/doi/10.1021/acscatal.1c04214.

> Additional figures and a table as described in the text (PDF)

■ AUTHOR INFORMATION

Corresponding Authors

WooChul Jung − *Department of Materials Science and Engineering, Korea Advanced Institute of Science and Technology (KAIST), Daejeon 34141, Republic of Korea;* ⓘ orcid.org/0000-0001-5266-3795; Email: wcjung@kaist.ac.kr

Raymond J. Gorte − *Department of Chemical and Biomolecular Engineering, University of Pennsylvania, Philadelphia, Pennsylvania 19104, United States;* ⓘ orcid.org/0000-0003-0879-715X; Email: gorte@seas.upenn.edu

Authors

Siwon Lee − *Department of Materials Science and Engineering, Korea Advanced Institute of Science and Technology (KAIST), Daejeon 34141, Republic of Korea; Department of Chemical and Biomolecular Engineering, University of Pennsylvania, Philadelphia, Pennsylvania 19104, United States*

Chao Lin − *Department of Chemical and Biomolecular Engineering, University of Pennsylvania, Philadelphia, Pennsylvania 19104, United States;* ⓘ orcid.org/0000-0003-0870-1138

Seunghyun Kim − *Department of Materials Science and Engineering, Korea Advanced Institute of Science and Technology (KAIST), Daejeon 34141, Republic of Korea*

Xinyu Mao − *Department of Chemical and Biomolecular Engineering, University of Pennsylvania, Philadelphia, Pennsylvania 19104, United States;* ⓘ orcid.org/0000-0002-8625-2617

Taeho Kim − *Center for Environment and Sustainable Resources, Korea Research Institute of Chemical Technology (KRICT), Daejeon 34114, Republic of Korea; Department of Advanced Materials & Chemical Engineering, University of Science and Technology (UST), Daejeon 34113, Republic of Korea*

Sang-Joon Kim − *Center for Environment and Sustainable Resources, Korea Research Institute of Chemical Technology (KRICT), Daejeon 34114, Republic of Korea; Department of Advanced Materials & Chemical Engineering, University of Science and Technology (UST), Daejeon 34113, Republic of Korea*

Complete contact information is available at:
https://pubs.acs.org/10.1021/acscatal.1c04214

Notes

The authors declare no competing financial interest.

■ REFERENCES

(1) Beniya, A.; Higashi, S. Towards dense single-atom catalysts for future automotive applications. *Nat. Catal.* **2019**, 2 (7), 590−602.

(2) Getsoian, A.; Theis, J. R.; Paxton, W. A.; Lance, M. J.; Lambert, C. K. Remarkable improvement in low temperature performance of model three-way catalysts through solution atomic layer deposition. *Nat. Catal.* **2019**, 2 (7), 614−622.

(3) Rodriguez, J. A.; Goodman, D. W. High-pressure catalytic reactions over single-crystal metal-surfaces. *Surf. Sci. Rep.* **1991**, 14 (1−2), 1−107.

(4) An, K.; Alayoglu, S.; Musselwhite, N.; Plamthottam, S.; Melaet, G.; Lindeman, A. E.; Somorjai, G. A. Enhanced CO oxidation rates at the interface of mesoporous oxides and Pt nanoparticles. *J. Am. Chem. Soc.* **2013**, 135 (44), 16689−16696.

(5) Kayaalp, B.; Lee, S.; Nodari, L.; Seo, J.; Kim, S.; Jung, W.; Mascotto, S. Pt Nanoparticles supported on a mesoporous (La,Sr)-(Ti,Fe)O$_{3-\delta}$ solid solution for the catalytic oxidation of CO and CH$_4$. *ACS Appl. Nano Mater.* **2020**, 3 (11), 11352−11362.

(6) Yoo, M.; Yu, Y.-S.; Ha, H.; Lee, S.; Choi, J.-S.; Oh, S.; Kang, E.; Choi, H.; An, H.; Lee, K.-S.; Park, J. Y.; Celestre, R.; Marcus, M. A.; Nowrouzi, K.; Taube, D.; Shapiro, D. A.; Jung, W.; Kim, C.; Kim, H. Y. A tailored oxide interface creates dense Pt single-atom catalysts with high catalytic activity. *Energy Environ. Sci.* **2020**, 13 (4), 1231−1239.

(7) Bunluesin, T.; Putna, E. S.; Gorte, R. J. A comparison of CO oxidation on ceria-supported Pt, Pd, and Rh. *Catal. Lett.* **1996**, *41* (1), 1−5.

(8) Jain, N.; Roy, A. Phase & morphology engineered surface reducibility of MnO_2 nano-heterostructures: Implications on catalytic activity towards CO oxidation. *Mater. Res. Bull.* **2020**, *121*, 110615.

(9) Duan, X. X.; Qu, Z. P.; Dong, C.; Qin, Y. Enhancement of toluene oxidation performance over $Pt/MnO_2@Mn_3O_4$ catalyst with unique interfacial structure. *Appl. Surf. Sci.* **2020**, *503*, 144161.

(10) Wang, M.; Zhang, L. X.; Huang, W. M.; Zhou, Y. J.; Zhao, H.; Lv, J.; Tian, J. J.; Kan, X. T.; Shi, J. L. Pt/MnO_2 nanosheets: facile synthesis and highly efficient catalyst for ethylene oxidation at low temperature. *RSC Adv.* **2017**, *7* (24), 14809−14815.

(11) Yu, X. H.; He, J. H.; Wang, D. H.; Hu, Y. C.; Tian, H.; He, Z. C. Facile controlled synthesis of Pt/MnO_2 nanostructured catalysts and their catalytic performance for oxidative decomposition of formaldehyde. *J. Phys. Chem. C* **2012**, *116* (1), 851−860.

(12) Onn, T. M.; Zhang, S. Y.; Arroyo-Ramirez, L.; Xia, Y.; Wang, C.; Pan, X. Q.; Graham, G. W.; Gorte, R. J. High-surface-area ceria prepared by ALD on Al_2O_3 support, Applied Catalysis B-Environmental. *Appl. Catal., B* **2017**, *201*, 430−437.

(13) van Ommen, J. R.; Goulas, A. Atomic layer deposition on particulate materials, Materials Today Chemistry. *Mater. Today Chem.* **2019**, *14*, 100183.

(14) Lu, J. L.; Fu, B. S.; Kung, M. C.; Xiao, G. M.; Elam, J. W.; Kung, H. H.; Stair, P. C. Coking- and sintering-resistant palladium catalysts achieved through atomic layer deposition. *Science* **2012**, *335* (6073), 1205−1208.

(15) Sudheeshkumar, V.; Lushington, A.; Sun, X. L.; Scott, R. W. J. Thermal stability of alumina-overcoated Au-25 clusters for catalysis. *ACS Appl. Nano Mater.* **2018**, *1* (12), 6904−6911.

(16) Duan, H. M.; You, R.; Xu, S. T.; Li, Z. R.; Qian, K.; Cao, T.; Huang, W. X.; Bao, X. H. Pentacoordinated Al^{3+}-stabilized active Pd structures on Al_2O_3-coated palladium catalysts for methane combustion. *Angew. Chem., Int. Ed.* **2019**, *58* (35), 12043−12048.

(17) Littlewood, P.; Liu, S.; Weitz, E.; Marks, T. J.; Stair, P. C. Ni-alumina dry reforming catalysts: Atomic layer deposition and the issue of Ni aluminate. *Catal. Today* **2020**, *343*, 18−25.

(18) Seo, J.; Tsvetkov, N.; Jeong, S. J.; Yoo, Y.; Ji, S.; Kim, J. H.; Kang, J. K.; Jung, W. Gas-permeable inorganic shell improves the coking stability and electrochemical reactivity of Pt toward methane oxidation. *ACS Appl. Mater. Interfaces* **2020**, *12* (4), 4405−4413.

(19) Lee, J.; Jackson, D. H. K.; Li, T.; Winans, R. E.; Dumesic, J. A.; Kuech, T. F.; Huber, G. W. Enhanced stability of cobalt catalysts by atomic layer deposition for aqueous-phase reactions. *Energy Environ. Sci.* **2014**, *7* (5), 1657−1660.

(20) Sarnello, E.; Lu, Z.; Seifert, S.; Winans, R. E.; Li, T. Design and characterization of ALD-based overcoats for supported metal nanoparticle catalysts. *ACS Catal.* **2021**, *11* (5), 2605−2619.

(21) Liang, X.; Li, J.; Yu, M.; McMurray, C. N.; Falconer, J. L.; Weimer, A. W. Stabilization of supported metal nanoparticles using an ultrathin porous shell. *ACS Catal.* **2011**, *1* (10), 1162−1165.

(22) Cao, L.; Lu, J. Atomic-scale engineering of metal-oxide interfaces for advanced catalysis using atomic layer deposition. *Catal. Sci. Technol.* **2020**, *10* (9), 2695−2710.

(23) Zhang, B.; Qin, Y. Interface tailoring of heterogeneous catalysts by atomic layer deposition. *ACS Catal.* **2018**, *8* (11), 10064−10081.

(24) Yang, J.; Cao, K.; Gong, M.; Shan, B.; Chen, R. Atomically decorating of MnO_x on palladium nanoparticles towards selective oxidation of benzyl alcohol with high yield. *J. Catal.* **2020**, *386*, 60−69.

(25) Yang, N.; Yoo, J. S.; Schumann, J.; Bothra, P.; Singh, J. A.; Valle, E.; Abild-Pedersen, F.; Nørskov, J. K.; Bent, S. F. Rh-MnO interface sites formed by atomic layer deposition promote syngas conversion to higher oxygenates. *ACS Catal.* **2017**, *7* (9), 5746−5757.

(26) Mao, X.; Lin, C.; Graham, G. W.; Gorte, R. J. A perspective on thin-film perovskites as supports for metal catalysts. *ACS Catal.* **2020**, *10* (15), 8840−8849.

(27) Lin, C.; Foucher, A. C.; Ji, Y.; Curran, C. D.; Stach, E. A.; McIntosh, S.; Gorte, R. J. Intelligent" Pt catalysts studied on high-surface-area $CaTiO_3$ films. *ACS Catal.* **2019**, *9* (8), 7318−7327.

(28) Mao, X.; Foucher, A. C.; Montini, T.; Stach, E. A.; Fornasiero, P.; Gorte, R. J. Epitaxial and strong support interactions between Pt and $LaFeO_3$ films stabilize Pt dispersion. *J. Am. Chem. Soc.* **2020**, *142* (23), 10373−10382.

(29) Mao, X. Y.; Foucher, A.; Stach, E. A.; Gorte, R. J. A study of support effects for CH_4 and CO oxidation over Pd catalysts on ALD-modified Al_2O_3. *Catal. Lett.* **2019**, *149* (4), 905−915.

(30) Onn, T. M.; Zhang, S.; Arroyo-Ramirez, L.; Chung, Y.-C.; Graham, G. W.; Pan, X.; Gorte, R. J. Improved thermal stability and methane-oxidation activity of Pd/Al_2O_3 catalysts by atomic layer deposition of ZrO_2. *ACS Catal.* **2015**, *5* (10), 5696−5701.

(31) Matam, S. K.; Kondratenko, E. V.; Aguirre, M. H.; Hug, P.; Rentsch, D.; Winkler, A.; Weidenkaff, A.; Ferri, D. The impact of aging environment on the evolution of Al_2O_3 supported Pt nanoparticles and their NO oxidation activity. *Appl. Catal., B* **2013**, *129*, 214−224.

(32) Klünker, C.; Balden, M.; Lehwald, S.; Daum, W. CO stretching vibrations on Pt(111) and Pt(110) studied by sumfrequency generation. *Surf. Sci.* **1996**, *360* (1), 104−111.

(33) Kale, M. J.; Christopher, P. Utilizing quantitative in situ FTIR spectroscopy to identify well-coordinated Pt atoms as the active site for CO oxidation on Al_2O_3-supported Pt catalysts. *ACS Catal.* **2016**, *6* (8), 5599−5609.

(34) Yashnik, S. A.; Ishchenko, A. V.; Dovlitova, L. S.; Ismagilov, Z. R. The nature of synergetic effect of manganese oxide and platinum in $Pt-MnO_x$-alumina oxidation catalysts. *Top. Catal.* **2017**, *60* (1), 52−72.

(35) Zhang, J.; Li, Y.; Wang, L.; Zhang, C.; He, H. Catalytic oxidation of formaldehyde over manganese oxides with different crystal structures. *Catal. Sci. Technol.* **2015**, *5* (4), 2305−2313.

(36) Cargnello, M.; Doan-Nguyen, V. V. T.; Gordon, T. R.; Diaz, R. E.; Stach, E. A.; Gorte, R. J.; Fornasiero, P.; Murray, C. B., Control of metal nanocrystal size reveals metal-support interface role for ceria catalysts. *Science* **2013**, *341* (6147), 771.

(37) Bunluesin, T.; Gorte, R. J.; Graham, G. W. CO oxidation for the characterization of reducibility in oxygen storage components of three-way automotive catalysts. *Appl. Catal., B* **1997**, *14* (1), 105−115.

(38) Su, X.; Cremer, P. S.; Shen, Y. R.; Somorjai, G. A. High-pressure CO oxidation on Pt(111) monitored with infrared-visible sum frequency generation (SFG). *J. Am. Chem. Soc.* **1997**, *119* (17), 3994−4000.

(39) Tran, S. B. T.; Choi, H.; Oh, S.; Park, J. Y. Defective Nb_2O_5-supported Pt catalysts for CO oxidation: Promoting catalytic activity *via* oxygen vacancy engineering. *J. Catal.* **2019**, *375*, 124−134.

(40) Song, H. C.; Oh, S.; Kim, S. H.; Lee, S. W.; Moon, S. Y.; Choi, H.; Kim, S. H.; Kim, Y.; Oh, J.; Park, J. Y. The effect of the oxidation states of supported oxides on catalytic activity: CO oxidation studies on Pt/cobalt oxide. *Chem. Commun.* **2019**, *55* (64), 9503−9506.

(41) Santos, V. P.; Pereira, M. F. R.; Órfão, J. J. M.; Figueiredo, J. L. The role of lattice oxygen on the activity of manganese oxides towards the oxidation of volatile organic compounds. *Appl. Catal., B* **2010**, *99* (1), 353−363.

(42) DeRita, L.; Dai, S.; Lopez-Zepeda, K.; Pham, N.; Graham, G. W.; Pan, X.; Christopher, P. Catalyst architecture for stable single atom dispersion enables site-specific spectroscopic and reactivity measurements of CO adsorbed to Pt atoms, oxidized Pt clusters, and metallic Pt clusters on TiO_2. *J. Am. Chem. Soc.* **2017**, *139* (40), 14150−14165.

(43) Pereira-Hernández, X. I.; DeLaRiva, A.; Muravev, V.; Kunwar, D.; Xiong, H.; Sudduth, B.; Engelhard, M.; Kovarik, L.; Hensen, E. J. M.; Wang, Y.; Datye, A. K. Tuning $Pt-CeO_2$ interactions by high-temperature vapor-phase synthesis for improved reducibility of lattice oxygen. *Nat. Commun.* **2019**, *10* (1), 1358.

(44) Ro, I.; Resasco, J.; Christopher, P. Approaches for understanding and controlling interfacial effects in oxide-supported metal catalysts. *ACS Catal.* **2018**, *8* (8), 7368−7387.

(45) van Deelen, T. W.; Hernández Mejía, C.; de Jong, K. P. Control of metal-support interactions in heterogeneous catalysts to enhance activity and selectivity. *Nat. Catal.* **2019**, *2* (11), 955−970.

(46) Cao, L.; Liu, W.; Luo, Q.; Yin, R.; Wang, B.; Weissenrieder, J.; Soldemo, M.; Yan, H.; Lin, Y.; Sun, Z.; Ma, C.; Zhang, W.; Chen, S.; Wang, H.; Guan, Q.; Yao, T.; Wei, S.; Yang, J.; Lu, J. Atomically dispersed iron hydroxide anchored on Pt for preferential oxidation of CO in H$_2$. *Nature* **2019**, *565* (7741), 631−635.